Int J Adv Manuf Technol (2018) 94:1073–1085
DOI 10.1007/s00170-017-0997-3

ORIGINAL ARTICLE

Nd:YAG pulsed laser welding of dissimilar metals of titanium alloy to stainless steel

Y. Zhang[1] · D. Q. Sun[1] · X. Y. Gu[1] · H. M. Li[1]

Received: 29 April 2017 / Accepted: 16 August 2017 / Published online: 24 August 2017

Abstract Pulsed laser welding of TC4 titanium (Ti) alloy to SUS301L stainless steel (SS) has been applied using pure Nb as an interlayer. Microstructures of the joints were analyzed by means of scanning electron microscopy (SEM), energy-dispersive spectroscopy (EDS), and X-ray diffraction (XRD). Mechanical properties of the joints were evaluated by tensile tests. Based on avoidance of the formation of Ti-Fe intermetallics in the joint, two welding processes for the Ti alloy-Nb-SS joint were introduced. One process was one pass welding involving creation of a joint with one weld zone and a reaction layer separated by remaining unmelted Nb. The weld was formed while the laser was acted on the Ti alloy-Nb interface, and simultaneously, the reaction layer was formed based on interdiffusion and eutectic reaction of Nb and Fe at the Nb-SS interface. The mechanical performance of the joint was determined by the reaction layer at the Nb-SS interface with a tensile strength of 370 MPa. The other was two pass welding involving creation of a joint with two weld zones separated by remaining unmelted Nb, while the laser beam was focused on the Ti alloy-Nb interface and the Nb-SS interface, respectively. At this point, the mechanical performance of the joint was determined by the weld zone formed at the Nb-SS interface with a tensile strength of 171 MPa.

Keywords TC4 titanium alloy · SUS301L stainless steel · Nb interlayer · Pulsed laser welding · Microstructure · Tensile strength

✉ X. Y. Gu
guxiaoyan821@sina.com

[1] Key Laboratory of Automobile Materials, School of Materials Science and Engineering, Jilin University, Changchun 130022, China

1 Introduction

Welded construction of titanium (Ti) alloy and stainless steel (SS) can reduce the weight of products, which is of great importance in spatial, aeronautic, and missile industries [1]. It is well known that there is difficulty in joining Ti alloy to steel due to a large amount of Ti-Fe intermetallics produced during welding, which affects the mechanical properties of joints seriously [2]. According to the Fe-Ti phase diagram [3], the solubility of Fe in Ti is very low (0.1 at.%, at room temperature), beyond which Fe-Ti intermetallic and then Fe_2Ti (600 and 1000 HV, respectively) begin to form [4]. These Ti-Fe intermetallics are highly brittle, causing conventional welding joints to crack spontaneously, due to thermal stress mismatch between the two base materials [5]. Therefore, suppressing the formation of brittle Ti-Fe intermetallics is the key to realizing reliable joining. There are mainly two types of welding method for joining Ti alloy to steel: diffusion bonding and fusion welding. Investigations of adding interlayers such as Ni [6, 7], Nb [8], and Ag [9] during diffusion bonding can partly prevent the interaction between Ti and Fe. However, some amounts of brittle Ti-Fe intermetallics were still formed and the maximum tensile strength of the joints was 258 MPa. Cu and their alloys are widely used as interlayer for bonding Ti alloy to steel because of their availability and relatively low cost. Cu does not produce brittle intermetallics when joined with iron, chromium, nickel, and carbon [10, 11]. Although Cu-Ti intermetallics are inevitably formed during fusion welding, the Cu interlayer can suppress an interaction between Ti and Fe. Therefore, using Cu as interlayer can greatly reduce the amount of the Ti-Fe intermetallics and subsequently realize the effective combination between dissimilar materials of Ti alloys and stainless steel. It is also reported that use of the Cu interlayer plays a role in reducing the amount of brittle Ti-Fe intermetallics during

fusion welding. At the same time, brittle Cu-Ti intermetallics, such as $CuTi_2$, were formed [12, 13]. Although these Cu-Ti intermetallics were found to be less brittle than the Ti-Fe phase, they still negatively impacted the ductility of the joint. In this case, the risk of embrittlement of the weld zone due to formation of Cu-Ti and Ti-Fe intermetallics is still high, and even when welding conditions are optimized, the weld zone-Ti alloy interface appears to be the weakest part of the joint due to formation of Ti-Fe intermetallics [14, 15]. Tensile strength of such joints rarely overpasses 350 MPa, which is much inferior to that of steels and Ti alloys. Based on the comprehensive analysis of information reported in the literature [12–17], it can be concluded that, adding whatever kind of interlayer during fusion welding of Ti alloy and steel, as long as the interlayer is completely melted, Ti and Fe elements will mix and react in the fusion pool. Thus, Ti-Fe intermetallics are inevitably formed. That is, Ti-Fe intermetallics in the weld can only be partly reduced by adding an interlayer during fusion welding, but cannot be completely eliminated if the interlayer is fully melted. Except for diffusion bonding and fusion welding, hot roll bonding also was used to realize the connection of Ti alloy and steel. Zongan et al. [18] obtained a highly qualified vacuum hot roll-bonded joint for titanium-stainless steel clad plate with an Nb interlayer. The Nb interlayer was chosen as a diffusion barrier because Nb does not form any intermetallics with Ti. Besides, Nb is malleable and ductile so it can conform easily to any joint configuration [19, 20]. According to Zongan's report, contact reaction of Fe and Nb can occur in a short time at the temperature of 1000 °C during the bonding process. At the same time, it can be concluded that there was no liquid produced during the contact reaction on the basis of their experimental parameters and results. The maximum shear strength of 396 MPa was obtained when bonding is carried out at 900 °C. Oliveira et al. [21] also pointed out that the Nb interlayer with a higher melting point than two dissimilar base materials had proven to be a successful diffusion barrier that did not allow mixing when joining NiTi to Ti alloy by laser welding. The average tensile strength of these joints was 300 MPa.

In view of the above analysis, pulsed laser welding of Ti alloy and SS using Nb as interlayer was proposed in this paper. The unmelted Nb interlayer was left in the joint after welding with the main objective of avoiding mixing of Ti and Fe so that the formation of Ti-Fe intermetallics was expected to be eliminated in the joint. Two welding processes termed as "one-pass welding" and "two-pass welding" were applied to acquire the joints. The relation between joint microstructures, mechanical properties, and fracture modes was discussed in detail. And the formation mechanism of the reaction layer in the joint during one-pass welding was elaborated especially.

2 Experimental procedure

2.1 Materials

The present paper reports the feasibility of pulsed Nb:YAG laser welding of Ti alloy to stainless steel through a 1-mm pure Nb interlayer. This 1-mm thickness of Nb was chosen to ensure that sufficient thickness of unmelted Nb was remained on joints to prevent diffusion and reaction of Ti and Fe. Meanwhile, the thickness should be suitable so that enough heat would be transferred to the Nb-SS interface to ensure the diffusion and reaction of Nb and Fe here. The base materials used in this experiment were TC4 Ti alloy and 301L stainless steel. Their chemical compositions and physical properties are given in Tables 1, 2, and 3. It can be seen that there are large differences in thermal conductivity and linear expansion coefficient between the two base materials, which would lead to large temperature gradient and thermal stress in the joint during welding process [22, 23]. The base materials were machined into 50 mm × 40 mm × 0.8 mm plates, and then cleaned with acetone before welding. A 1-mm-thick Nb sheet (99.99 at. %) was adopted as interlayer and placed on the contact surface of the base material fixed in fixture.

2.2 Welding method

Nd:YAG pulsed laser was used with an average power of 1.05 kW, wavelength of 1.064 μm, and beam spot diameter of 0.1 mm. A schematic diagram of the welding process is shown in Fig. 1, where a good fit-up between Ti alloy-Nb-SS was required to prevent gaps and ensure adequate heat transfer to form a joint. Two different welding processes are applied, and welding conditions of joints are provided below.

One-pass welding In order to ensure that the Nb interlayer was not completely melted, the laser beam was focused on the Ti alloy plate 0.2 mm away from the Ti alloy-Nb interface (Fig. 1a). The welding process parameters were as follows: laser beam current of 80 A, pulse duration of 15 ms, defocusing distance of + 2 mm, pulse frequency of 4 Hz, welding speed of 100 mm/min.

Two-pass welding During the first pass, Ti alloy was welded to Nb sheet with the laser beam focused on the Ti alloy-Nb

Table 1 Main chemical compositions of 301 L stainless steel (at.%)

Si	Mn	P	S	Cr	Ni	N	Fe
< 1.00	< 2.00	< 0.045	0.03	16.00–18.00	6.00–8.00	< 0.20	Bal

Table 2 Main chemical compositions of TC4 Titanium alloy (at.%)

Al	V	Fe	C	N	H	O	Ti
6.05	4.02	0.14	0.02	0.02	0.006	0.12	Bal

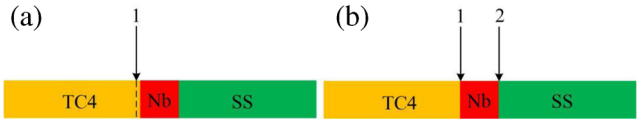

Fig. 1 Schematic diagram of the welding process. **a** Joint A performed with one-pass welding. **b** Joint B performed with two-pass welding

interface, and during the second pass (immediately after the first one), Nb sheet was welded to SS with the laser beam focused on the Nb-SS interface (Fig. 1b). The welding process parameters were as follows: laser beam current of 63 A, pulse duration of 8 ms, defocusing distance of + 2 mm, pulse frequency of 6 Hz, welding speed of 250 mm/min.

2.3 Characterization methods

The cross sections of joints were polished and etched in the reagent with 2 ml concentrated HNO_3 and 6 ml concentrated HF. The microstructure of joints were studied by optical microscopy (Axio Scope, Zeiss), scanning electron microscopy (SEM, S-3400) with fast energy-dispersive spectrum EDS analysis, and selected area XRD (X'Pert^3 Powder) analysis. Vickers microhardness tests for the weld were carried out with a 10-s load time and a 200-g load. Microhardness of the reaction layer was also evaluated by using the nanoindentation (G200 Micro/Nano mechanical) test. Tensile strength of the joints was measured by using a universal testing machine (MTS Insight 10 kN) with cross head speed of 2 mm/min.

3 Results and discussion

3.1 Characterization of joint A

3.1.1 Macro-characteristics

Figure 2a presents the surface feature of joint A. The laser beam was focused on the Ti alloy near the Ti alloy-Nb interface during welding so that the Nb interlayer was not completely melted. The melted Ti alloy and Nb interlayer formed the welding pool, and the weld zone was produced during subsequent cooling. Figure 2b presents the cross section of joint A. It is obvious that the joint consisted of three distinct regions, namely, the weld zone formed at the Ti alloy-Nb interface, unmelted Nb, and the reaction layer formed at the Nb-SS interface. The weld zone had an average width of approximately 1.3 mm, and the reaction layer had an average width of approximately 50 μm. The top and bottom of the weld zone was similar in width. The cross section of the weld zone looks like an X shape. In addition, the width of unmelted Nb was 200 μm and almost 20% of initial sheet thickness, which indicated a larger amount of Nb melted in the weld zone. This is mainly due to the large heat input for joint A to ensure that the reaction layer was formed at the Nb-SS interface. The unmelted part of the Nb interlayer acted as a heat sink due to its high thermal conductivity absorbing a significant amount of energy from the welding pool and transferring it to the SS side [21]. Hence, the Nb-SS interface had a high temperature during welding although it was not subjected to laser radiation. The temperature was high enough to promote atomic interdiffusion. Furthermore, as heated, expansions of the Nb interlayer and SS was non-uniform and thermal stress was produced, which helped to obtain an intimate contact between Nb and SS. The high temperature and the intimate contact at the Nb-SS interface provided favorable conditions for atomic interdiffusion, which subsequently led to eutectic reaction between Nb and Fe at the Nb-SS interface. Therefore, a reaction layer was formed originated from interdiffusion of Nb and Fe at the interface between the unmelted interlayer and SS. As a result, a joint was obtained comprising a weld zone formed by fusion welding at the Ti alloy-Nb interface and a reaction layer formed by interdiffusion and eutectic reaction of Nb and Fe at the Nb-SS interface. The unmelted part of the Nb interlayer also acted as a diffusion barrier between Ti and Fe to avoid the Ti-Fe intermetallics. Additionally, the unmelted Nb interlayer was beneficial to relieve and accommodate the thermal stress in the Ti alloy-SS joint, which could help to improve the mechanical properties of the joints. It should be noted that precise control of the laser spot position is crucial to obtain a sound weld. If the laser spot is far away from the Nb interlayer, eutectic reaction of Nb and Fe at the Nb-SS interface cannot take place.

Table 3 Physical properties of TC4 titanium alloy and 301L stainless steel

Material	Melting point/°C	Tensile strength/MPa	Specific heat capacity/(J kg^{-1} K^{-1})	Thermal conductivity/(W m^{-1} K^{-1})	Linear expansion coefficient (10^{-6} K^{-1})
TC4	1650	895	536	6.4	8.7
SUS301L	1450	550	500	16.3	16.9

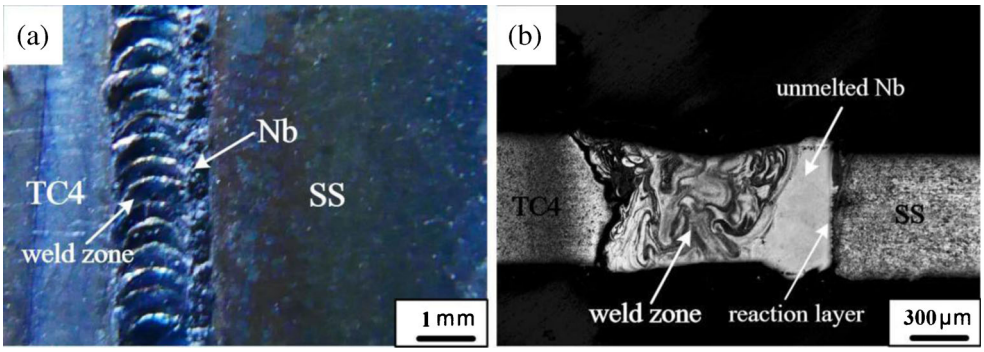

Fig. 2 Optical image of joint A obtained by one-pass welding. **a** Surface feature. **b** Cross section

3.1.2 Microstructure analysis

Figure 3 shows the optical image of the weld zone of joint A, and no defects were observed in it. Under the action of pulsed laser, the melted Nb interlayer and Ti alloy mixed and reacted with each other. As shown in Table 4, Ti and Nb, as two main elements, were detected in the weld. However, Fe element was not found, which indicated the absence of Ti-Fe intermetallics. According to the Ti-Nb binary phase diagram, no intermetallics will be formed from Ti and Nb. Moreover, formation of intermetallics between Nb and other alloying elements of Ti-6Al-4V in the melt pool is not reasonable [24]. Based on EDS results and the Ti-Nb binary phase diagram, the main microstructure of this weld zone was (Ti, Nb) solid solution. Furthermore, it is noted that there were some zones like islands in the upper part of the weld zone as shown in Fig.

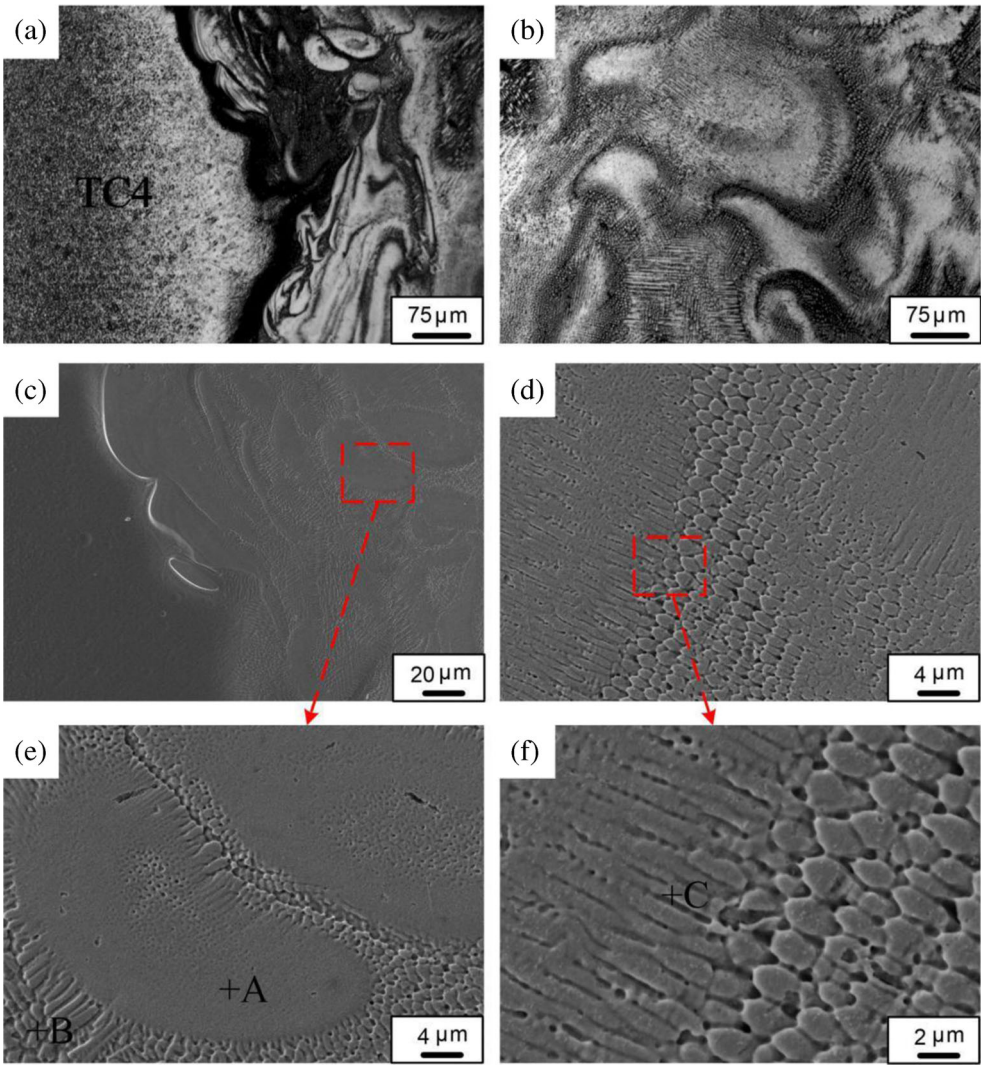

Fig. 3 Microstructures in the weld zone of joint A. **a** Optical image of the fusion line near Ti alloy. **b** Optical image of the weld zone centerline. **c** SEM image of the fusion line near Ti alloy. **d** SEM image of the weld centerline. **e** Refers to the area in c. **e** Refers to the area in **d**

Table 4 Compositions of main elements in the weld zone of joint A (at.%)

	Nb	Ti	Al	V
A	75.42	21.52	2.62	0.45
B	49.81	44.86	4.31	0.98
C	48.52	45.38	5.88	0.13

3a, c, e. It can be seen in Table 4 that zone A in the island had a concentration of 75 at.% Nb and zone B near the island had a concentration of 49 at.% Nb. This indicated that the constituents of (Ti, Nb) solid solution in this weld zone at the Ti alloy-Nb interface were non-uniform. Since the weld zone was composed of a partly overlapping welding spot from a single pulse, the formation of one welding spot was equivalent to a stir for the molten pool and the intense flow was formed in the molten pool. According to Torkamany et al. [25], when pulsed laser welding was applied to connect niobium with Ti-6Al-4V, an intense flow was formed in the upper part of the molten pool and Ti and Nb have been thrown to the opposite side of the keyhole. It is also reported that temperature and surface tension gradients in the molten pool lead to the flow of the liquid metal in different directions during pulsed laser welding [26, 27], which facilitated the non-uniform liquid phase composition in the molten pool. Simultaneously, since the heating and solidification process in the weld zone was faster for pulsed laser welding, rapid solidification exacerbated the inhomogeneous distribution of microstructure in the weld zone. Furthermore, it can be seen from Fig. 3b, d, f that (Ti, Nb) solid solution presented columnar grains and granular, which implied the two growth directions of the phase.

The optical image of the reaction layer at the Nb-SS interface is shown in Fig. 4a. A SEM image of the reaction layer is shown in Fig. 4b. It can be observed that the reaction layer contained three zones marked as I, II, and III sorted by their morphologies and colors. Figure 4c presents the elemental distribution profile across the Nb-SS interface marked with three zones. EDS analysis was applied to these zones to measure the compositions of the reaction products, and the results are listed in Table 5. It is seen in Fig. 4b, e that zone I presents characteristics of the eutectic microstructure. This means liquid was produced in this zone during welding. Moreover, according to EDS analysis results in Table 5, the composition at point A was 55.67 at.% Fe and 20.21 at.% Nb. Combined with the binary phase diagram of Fe-Nb, this composition was hypereutectic. So it can be concluded that at point A, the (Fe_2Nb) phase was primarily precipitated from liquid during cooling. Then the composition of Nb in the residual liquid increased, which resulted in the eutectic reaction (L → + δ-Fe). Consequently, the main microstructure of point A were phase and + δ-Fe eutectic. The composition at point B were 65.42 at.% Fe and 7.01 at.% Nb. This composition was hypoeutectic, and δ-Fe was primarily precipitated from liquid. Then the composition of Fe in the residual liquid increased, which resulted in the eutectic reaction (L → + δ-Fe). In the subsequent cooling process, allotropy transformations (δ-Fe → γ-Fe and γ-Fe → α-Fe) occurred and α-Fe was formed. Thus, the reaction process of zone I was explained as the hypoeutectic reaction and the eutectic reaction, forming an obvious liquid eutectic microstructure. The main microstructures of zone I were Fe_2Nb, α-Fe, and Fe_2Nb + α-Fe. As shown in Fig. 4d, f, zone II and zone III were reaction layers

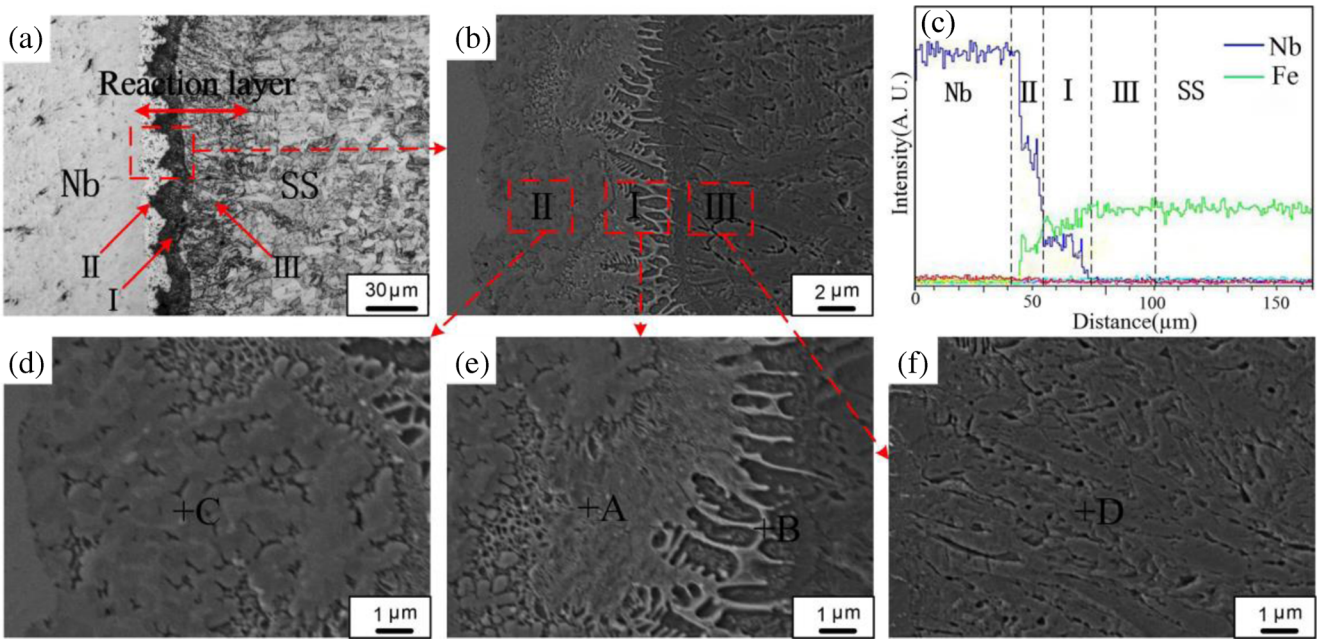

Fig. 4 Microstructures and linear SEM-EDS in the reaction layer of joint A. **a** Optical image of the reaction layer. **b** SEM image of the reaction layer. **c** Linear SEM-EDS of the reaction layer. **d** Refers to zone II in **b**. **e** Refer to zone I in **b**. **f** Refer to zone III in **b**

Table 5 EDS analysis of reaction layer in joint A

Region	Composition (at.%)						Potential phases
	Ti	Fe	Nb	V	Ni	Cr	
A		55.67	20.21		7.07	14.04	Fe_2Nb + α-Fe
B		65.42	7.01		6.06	18.34	α-Fe + Fe_2Nb
C		44.45	40.19		3.24	12.12	Fe_7Nb_6
D		72.68	0.42		8.37	18.54	α-Fe

formed by element diffusion. The composition at point C of zone II was 44.45 at.% Fe and 40.19 at.% Nb with the atomic ratio of Fe/Nb close to the stoichiometric ratio of Fe_7Nb_6. Therefore, the main microstructure of zone II was defined as Fe_7Nb_6. The composition of Nb at point D of zone III was 0.42 at.% Nb and 72.68 at.% Fe. Based on the Fe-Nb diagram, the microstructure in zone III was ferrite (α-Fe). In addition, it can be seen in Fig. 4c that in zone II there was a high Nb content and some amount of Fe element diffused into this zone. There was a high Fe content in zone III and very little amount of Nb element diffused into this zone. As is known, the γ-Fe in SS has an fcc crystal structure, and Nb has a bcc crystal structure with a more open space [28]. It was also reported that in [29], Fe was found to have a faster diffusion rate than Nb in Fe_7Nb_6 and Fe_2Nb phases. Therefore, a larger amount of Fe element diffused into the Nb side than that of the Nb element diffused into SS side. In this case, Fe-Nb intermetallics were formed at the Nb side and no Fe-Nb intermetallics but α-Fe was formed at the SS side. Therefore, the microstructure of the reaction layer was Nb/Fe_7Nb_6/Fe_2Nb+α-Fe/α-Fe/SS.

A schematic of a formation process of the reaction layer is presented in Fig. 5. When the laser beam was focused near the Ti alloy-Nb interface, the temperature at the Nb-SS interface increased due to heat conduction. Firstly, at the Nb-SS interface physisorption and chemisorption may proceed at the same time. The adsorption process was the precondition of interatomic interactions, which needed enough activation energy. The high temperature of the Nb-SS interface provided the activation energy. Thus, Nb and Fe atoms gathered at the Nb-SS interface under high interface temperature (Fig. 5a). The interdiffusion of Nb and Fe atoms occurred until eutectic composition was acquired, and liquid phase was formed by the eutectic reaction. At this moment, the dissolution of Nb and SS into the eutectic liquid phase occurred under the high concentration gradient, and this caused the composition in the liquid phase to vary from the eutectic point as indicated in Fig. 5b. Also because of the fast heating and cooling during the pulsed laser welding process, the diffusion in the liquid was not sufficient and the composition distribution in the liquid was uneven. In the subsequent cooling process, the liquid phase with different compositions would experience different reactions. Typical reactions were explained as points A and B in zone I in the previous paragraph. When the temperature decreased, solidification started with nucleation of primary phases. Both primary Fe_2Nb and α-Fe were formed in the microstructure, because the solid solubility at the liquid/solid interface was saturated. The chemical composition of the liquid was changed toward the eutectic point. Then, a eutectic microstructure (Fe_2Nb + α-Fe) was formed by eutectic reaction (Fig. 5c). Accompanied with dissolution of solid Nb and SS into the liquid, Fe and Nb atoms would diffuse from the liquid into Nb and SS substrates, respectively, which formed the reaction layer of zone II and zone III (Fig. 5d). This process was controlled by atomic solid diffusion.

3.1.3 Microhardness and nano-indentation tests

As shown in Fig. 6a, the microhardness distribution in joint A was non-uniform. But overall, the microhardness distribution in the weld zone was relatively uniform and the average value was 360 HV which was slightly above the Ti alloy. The TC4

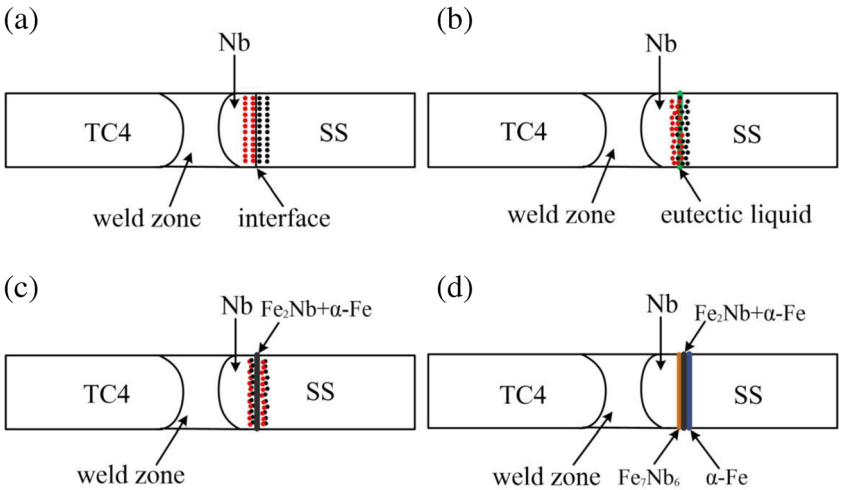

Fig. 5 The schematic of the formation process of a reaction layer. **a** Initial state of the Nb-SS interface: adsorption. **b** Dissolution and diffusion of Nb and Fe atoms into eutectic liquid. **c** The formation of the liquid/solid interface. **d** The formation of a reaction layer

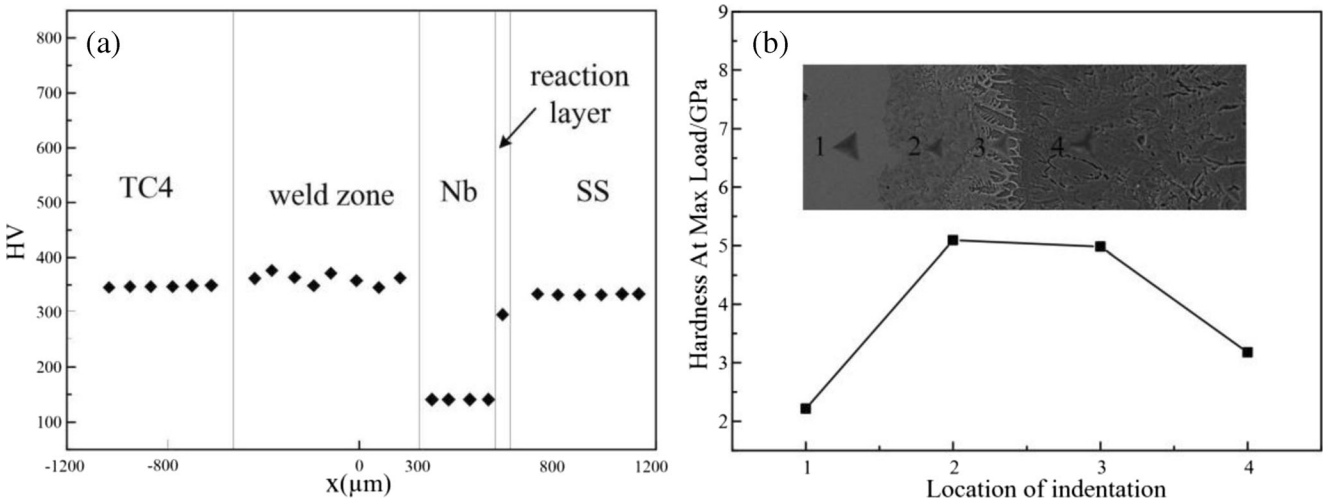

Fig. 6 Microhardness and nano-indentation of joint A analysis results. **a** Vickers microhardness measurements at the semi-height of joint A (zero point situated in the center of joint A). **b** The distribution of nano-indentation at the Nb-SS interface of joint A

Ti alloy has a similar hardness to 301L stainless steel, and the hardness of the Nb interlayer was low because it was a simple metal. The hardness of the reaction layer was higher than that of the Nb interlayer. This was mainly attributed to Nb-Fe intermetallics. But the reaction layer had relatively lower hardness compared with the weld zone and base materials. Therefore, it can relatively deform easily to reduce the inner stress of joint A during pulsed laser welding. Since the reaction layer's width of joint A was less than 0.1 mm, indentation of the microhardness which covers a larger area could not reflect the distribution of the reaction layer hardness well. In this experiment, a nano-indentation test was applied. The nano-indentation at max load obtained also reflects the value of the microhardness. As shown in Fig. 6b, indentation loads obtained at the Nb-SS interface were non-uniform. The maximum indentation modulus is located in zone II and the second highest point located in zone I. As mentioned above, the main intermetallics of zone II and zone I were Fe_7Nb_6 and Fe_2Nb. Therefore, it can be concluded that the hardness of Fe_7Nb_6 is higher than that of Fe_2Nb. This is mainly because the crystal structure of hcp is dominant in Fe_7Nb_6; slip systems are more limited and with sound wear resistance. In addition, the hardness of zone I and zone II was obviously higher than that of residual Nb and zone III. It means that of all three zones, zone II has the biggest brittleness. This was resulted from Fe_7Nb_6 and Fe_2Nb in the reaction layer as mentioned above. Therefore, the nano-indentation results were in accordance with the microstructure analysis and the regions rich in Fe-Nb intermetallics exhibited higher hardness.

3.1.4 Tensile tests and fractography

The maximum tensile strength and elongation of joint A was 370 MPa and 1%, respectively (Fig. 7a). The tensile strength of joint A was higher than that of most diffusion bonding joints between Ti alloy and stainless steel. The ultimate tensile strength of the Nb interlayer was close to 400 MPa, so the tensile strength of joint A matched the ultimate theoretical strength of the Nb interlayer. As shown in Fig. 7b, fracture occurred in the reaction layer at the Nb-SS interface and fracture passed through zone II and zone I. SEM images of the fracture surfaces are presented in Fig. 7c–f. As shown in Fig. 7c, d, fracture surfaces were characterized by a large area of cleavage tongue and cleavage fan. As shown in Fig. 7e, f, fracture surfaces were characterized by a number of secondary crack zones and a big naphthalene pattern. This means the fracture mode of the joint was brittle fracture. EDS analysis of the fracture surface in the Nb side showed a composition of 37.52 at.% Nb and 42.15 at.% Fe, which indicated existence of the Fe_7Nb_6 phase. EDS analysis of the fracture surface in the SS side showed a composition of 26.94 at.% Nb and 56.49 at.% Fe, which indicated existence of the Fe_2Nb phase. Moreover, as shown in Fig. 8, XRD analyses of the fracture surface in the Nb side detected Fe_7Nb_6 phase and those in the SS side detected Fe_7Nb_6 and Fe_2Nb phases. This confirmed the presence of a large number of Nb-Fe intermetallics at fracture surfaces. As mentioned in Sect. 3.1.3, experimental results show that the maximum indentation modulus is located in zone II with a microstructure of Fe-Nb intermetallics. Although these Fe-Nb intermetallics were still hard, they had relatively lower hardness compared with Ti-Fe intermetallics. Therefore, it can relatively deform easily to reduce the residual stresses in the inner part of the Nb-SS interface. It should be noted that although there was no Ti-Fe intermetallics in the joint, Fe_7Nb_6 and Fe_2Nb also belong to a kind of hard and brittle intermetallics. It easily led to stress concentration, which resulted in the failure in the tensile test.

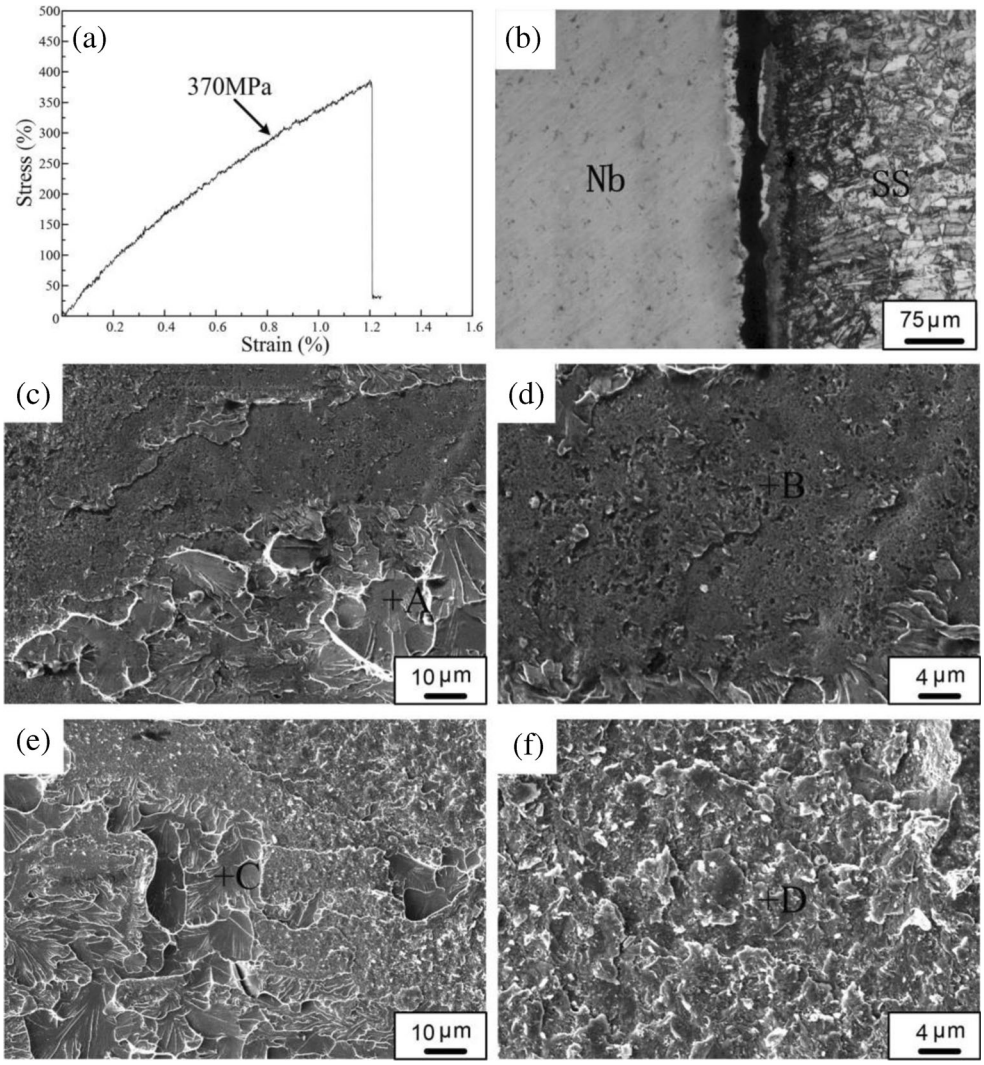

Fig. 7 Microstructures near the fracture location and tensile test curves of joint A. **a** Tensile test curves of joint. **b** Fracture location of joint. **c** Fracture surface of the Nb side. **d** Refer to the upper part in **c**. **e** Fracture surface of the SS side. **f** Refers to the upper part in **e**

Based on the above analysis on joint A, it can be concluded that the reaction layer at the Nb-SS interface becomes the weak zone of the joint. The weld zone at the Ti alloy-Nb interface has a higher strength than the reaction layer at the Nb-SS interface. It can be assumed that the mechanical property of the Ti alloy-Nb-SS joint could be improved if the

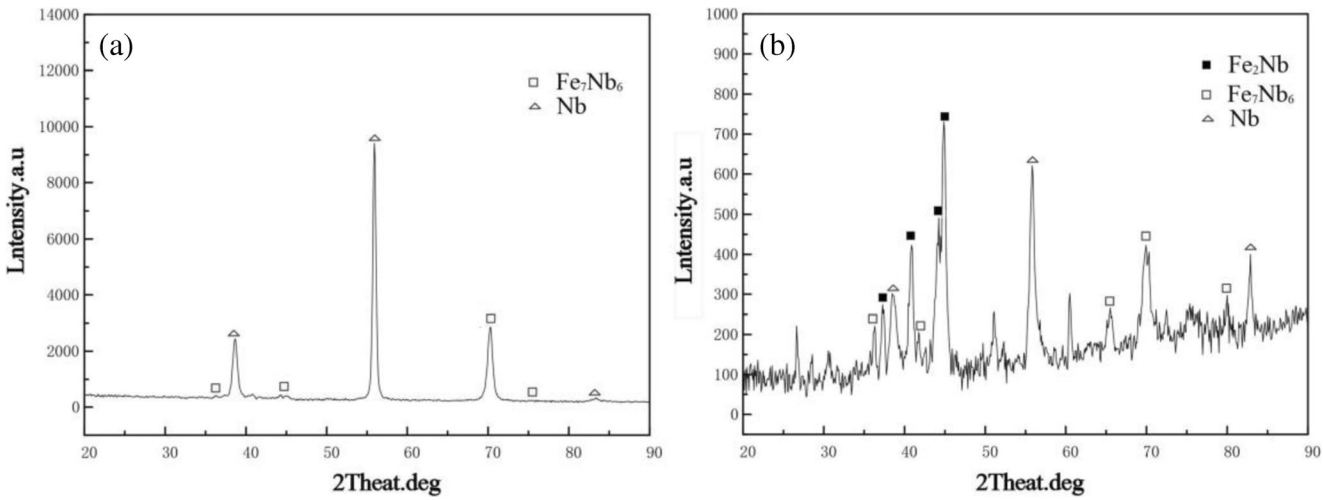

Fig. 8 XRD analysis results of fracture surfaces in joint A. **a** Nb side. **b** SS side

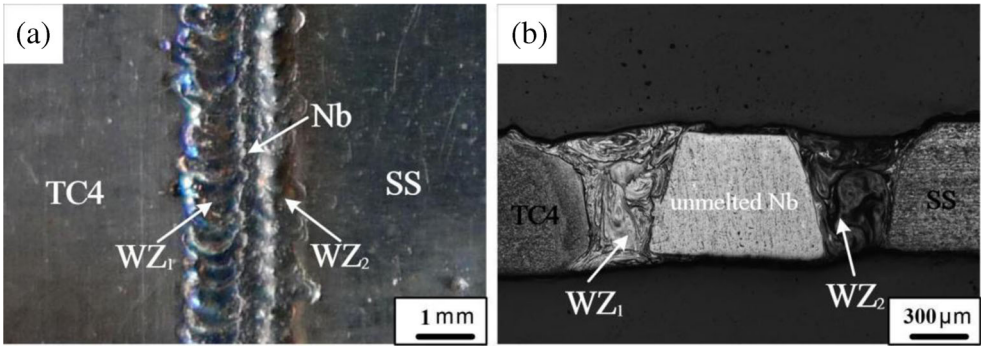

Fig. 9 Optical image of joint B obtained by two-pass welding. **a** Surface feature. **b** Cross section

interlayer Nb is not completely melted during welding. Another welding process proposed the premise of keeping the Nb interlayer partly melted. During welding, the laser beam was focused on the Ti alloy-Nb interface and Nb-SS interface, respectively. In this case, two weld zones are obtained. Compared with joint A, the reaction layer was replaced with the weld zone at the Nb-SS interface, and that was how we got joint B.

3.2 Characterization of joint B

3.2.1 Macro-characteristics

Figure 9a presents the surface feature of joint B. It can be seen that not only two weld zones were produced but also a residual unmelted Nb interlayer was situated between them. Figure 9b presents the cross section of joint B. It is obvious that the joint

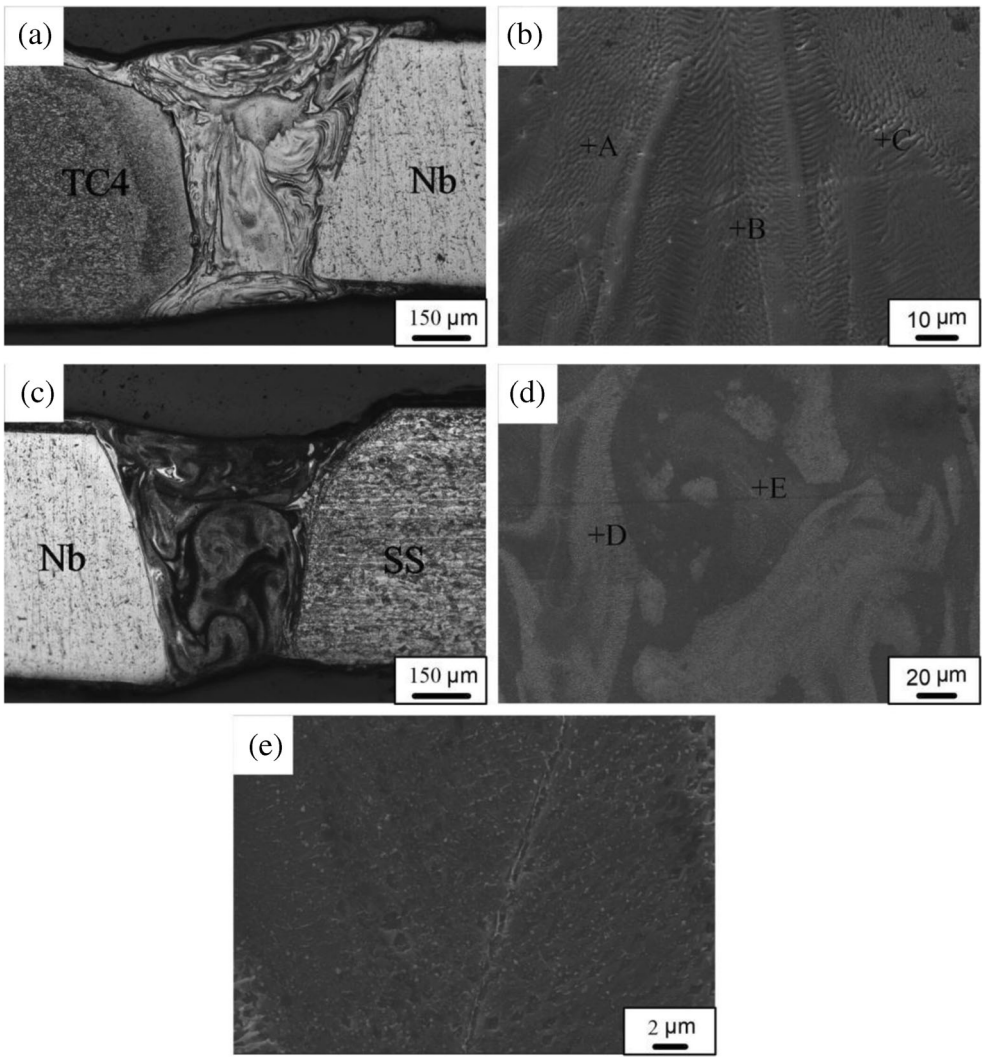

Fig. 10 Microstructures of joint B. **a** Optical image of WZ_1. **b** SEM image of WZ_1. **c** Optical image of WZ_2. **d** SEM image of WZ_2. **e** Crack of WZ_2

Table 6 EDS analysis of different zones in joint B

Region	Composition (at.%)							Potential phases
	V	Al	Ti	Nb	Fe	Ni	Cr	
A	2.83	9.52	75.11	12.54				(Ti, Nb)
B	2.53	9.01	75.38	13.08				(Ti, Nb)
C	2.61	8.68	72.24	16.47				(Ti, Nb)
D				5.81	70.07	5.46	18.66	γ-Fe
E				22.67	58.79	5.05	13.49	Fe_2Nb

consisted of three distinct regions, namely, WZ_1 formed at the Ti alloy-Nb interface, unmelted Nb, and WZ_2 formed at the Nb-SS interface. Meanwhile, the width of unmelted Nb was 750 μm and almost 75% of initial sheet thickness, which indicated a lower amount of Nb melted in joint B. The width of unmelted Nb was far above unmelted V of joint A. As can be seen from Fig. 9b, the cross section of WZ_1 and WZ_2 looked like an inverted trapezoid. This is due to the low heat input during welding to ensure that the V interlayer was not completely melted and to guarantee the existence of the unmelted V interlayer in the joint. Compared with joint A, with reduction of heat input, the cross section of the weld zone of the Ti alloy-Nb interface transformed from X shape to near trapezoid. The relatively thick unmelted Nb interlayer acted as a barrier to mix the two base materials, which prevented the formation of brittle Ti-Fe intermetallics.

3.2.2 Microstructure analysis

The optical image of WZ_1 at the Ti alloy-Nb interface is shown in Fig. 10a, and no defect was observed in it. A SEM image of WZ_1 is shown in Fig. 10b. It can be seen that WZ_1 consisted of cellular crystal. EDS analysis results in Table 6 show that the average compositions of Ti and Nb in WZ_1 were 75 and 14 at.%, respectively. Based on the EDS results and the Ti-Nb binary phase diagram, the main microstructure of WZ_1 was (Ti, Nb) solid solution. XRD analysis also confirmed the presence of (Ti, Nb) solid in WZ_1 (Fig. 11a). As can be seen from Fig. 10b, WZ_1 was composed by continuous and uniform solid solutions of (Ti, Nb) having a cellular microstructure. Compared with the weld zone of joint A, the microstructure of WZ_1 basically had no changes.

The optical image of WZ_2 at the Nb-SS interface is shown in Fig. 10c. A SEM image of WZ_2 is shown in Fig. 10d. It can be seen that WZ_2 was composed of various zones, marked as D and E, which were different in color. Based on the EDS analysis results in Table 6, zone D with white color had a concentration of 70 at.% Fe and 18 at.% Cr. Zone E with gray white color had a concentration of 23 at.% Nb and 58 at.% Fe. This means the main composition of zone D was close to SUS 301L stainless steel and the atomic ratio of Fe/Nb in zone E was close to the stoichiometric ratio of Fe_2Nb. In the meantime, XRD of WZ_2 showed the presence of γ-Fe and Fe_2Nb (Fig. 11d). Based on the EDS results and XRD analysis result, it can be conformed that WZ_2 was composed of γ-Fe and Fe_2Nb. According to the existing experimental data, it also can be found that in the weld adjacent to the Nb interlayer, content of Nb was higher than that in the weld centerline and

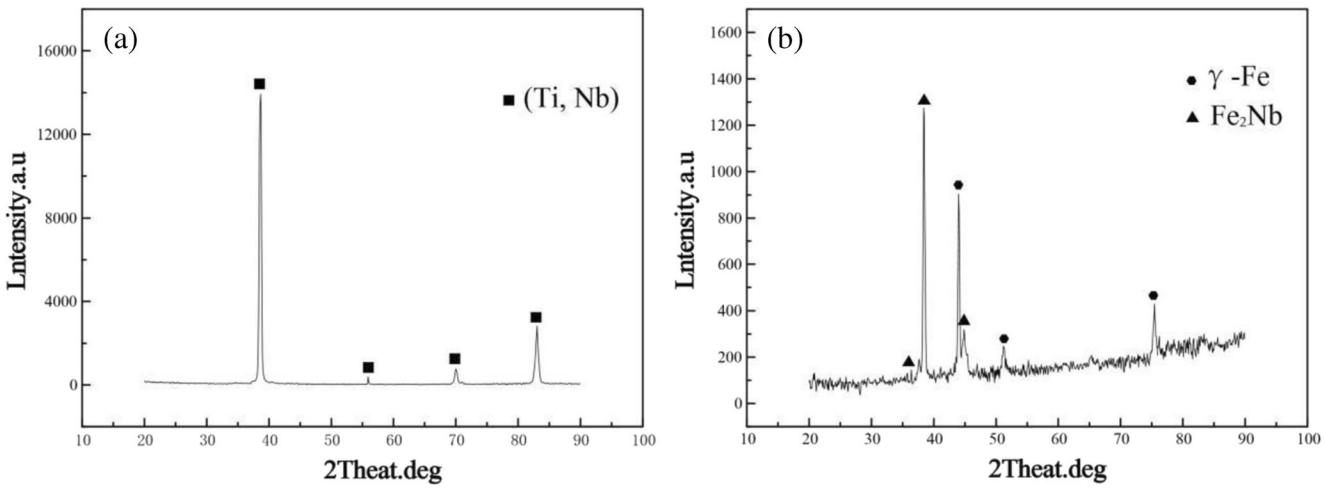

Fig. 11 XRD analysis results of joint B. **a** WZ_1. **b** WZ_2

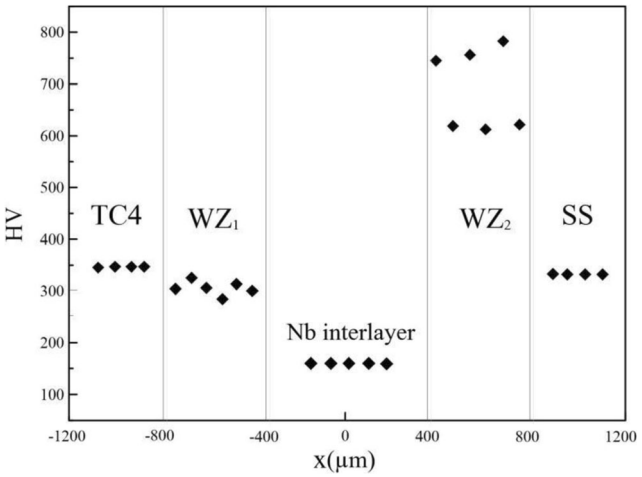

Fig. 12 Vickers microhardness measurements at the semi-height of joint B (zero point situated in the center of joint B)

that adjacent to stainless steel. At the same time, the Nb-Fe intermetallic layer with a certain width was continuously distributed along the weld adjacent to the Nb side. Besides, it was found that there were some γ-Fe rich zones mainly characterized in the weld adjacent to the fusion line adjacent to the stainless steel side. Moreover, according to EDS analysis results in Table 6, Fe was not found in WZ_1 and Ti was not detected in WZ_2, which indicated that the unmelted part of the Nb interlayer acted as a diffusion barrier and inhibited the reaction of Ti and Fe. In addition, some cracks were found in WZ_2 (Fig. 10e). This was attributed to high residual stresses in the joint and stress concentration in this region induced by a great difference between γ-Fe and Fe_2Nb.

3.2.3 Microhardness tests

As shown in Fig. 12, the microhardness distribution in WZ_1 was relatively uniform and the average value was 300 HV, which was slightly below the Ti alloy. Compare with the weld zone of joint A, the microhardness of WZ_1 of joint B decreased due to a low concentration of Nb (14 at.%) in it. As mentioned above, there was a relatively high concentration of Nb (48 at.%) in the weld zone of joint A. Therefore, probably due to the solution hardening of (Ti, Nb) by Nb, the hardness of (Ti, Nb) solid solution also showed an upward trend with increasing content of Nb element. At the same time, the microhardness distribution across WZ_2 was non-uniform. The maximum microhardness in WZ_2 was up to 790 HV, which was 240% of initial SUS 301L. The difference between the maximum and minimum microhardness was up to 300 HV. This resulted from the non-uniform microstructure of γ-Fe and Fe_2Nb in WZ_2. Therefore, the microhardness results were in accordance with the microstructure analysis and the regions rich in Fe-Nb intermetallics which exhibited higher hardness. The microhardness variance between γ-Fe and Fe_2Nb may cause a large stress concentration. This would have an adverse impact on the mechanical property of WZ_2.

3.2.4 Tensile tests and fractography

The maximum tensile strength and elongation of joint B was 171 MPa and 0.6%, respectively (Fig. 13a). When joint B was subjected to tensile test, the fracture took place at the

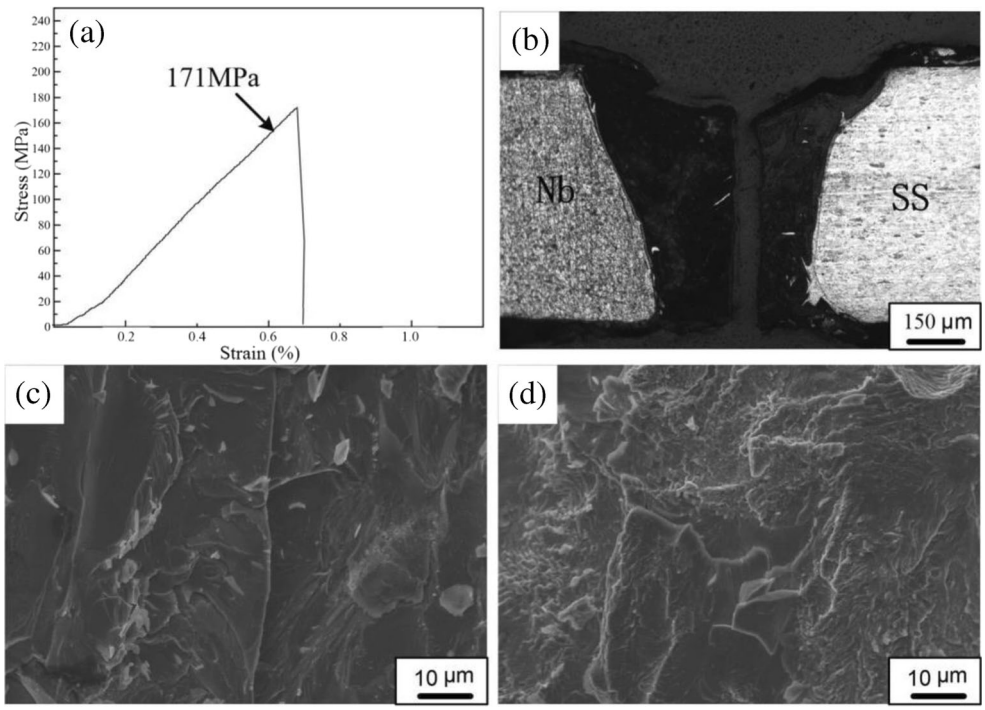

Fig. 13 Microstructures near the fracture location and tensile test curves of joint B. **a** Tensile test curves of joint. **b** Fracture location of joint tensile test. **c** Fracture surface of the Nb side. **d** Fracture surface of the SS side

centerline of WZ_2 (Fig. 13b). As shown in Fig. 13c, d, fracture surfaces were characterized by a lot of cleavage facet crack zones and cleavage planes. Furthermore, obvious river patterns on the cleavage plane were observed. This means the fracture mode of the joint is brittle fracture. EDS analysis of the fracture surface in the Nb side showed a composition of 27.75 at.% Nb and 53.29 at.% Fe, which indicated existence of Fe_2Nb phase. EDS analysis of the fracture surface in the SS side showed a composition of 74 at% Fe and 18 at.% Cr, which indicated existence of γ-Fe. It can be concluded that the joint fractured in the γ-Fe and Fe_2Nb continuous compound zone. As mentioned in Sect. 3.2.3, the hardness difference between γ-Fe and Fe_2Nb was great, which easily led to great stress concentration and subsequent failure in the tensile test. The underlying cause of the low tensile strength (only 171 MPa) of joint B was made up of too many Nb-Fe intermetallics in WZ_2. These Nb-Fe intermetallics caused spontaneous cracking in WZ_2 of the Nb-SS interface, which impaired the mechanical properties of joint B.

The above experimental results showed that the Nb interlayer and the stainless steel are bonded by a reaction layer with microstructure of Nb-Fe intermetallics formed in joint A although only one-pass laser welding was applied on the Ti alloy-Nb interface. On the other hand, large areas of γ-Fe and Nb-Fe intermetallics were formed in WZ_2 of joint B by two-pass welding and the propagating of cracks was formed during cooling, which would pose a very great stress concentration and significantly reduce the mechanical properties of WZ_2. As long as the laser beam was acted on the Nb-SS interface, a large amount of Nb and SS would melt, and a large amount of Nb-Fe intermetallics was inevitably formed. Experimental results showed that the Ti alloy and Nb interlayer formed a solid solution at the Ti alloy-Nb interface, thus enabling good metallurgical bonding. Nb-Fe intermetallics formed at the Nb-SS interface would make the crack sensitivity of joint increased and thus mechanical property would be decreased. Nb-Fe intermetallics were the major factor of fracture failure of Ti-Nb-SS joints for one-pass welding and two-pass welding. Choosing V as interlayer with two-pass welding might avoid formation of intermetallics in the Ti-SS joint, and it can be expected to further improve the mechanical property of the joint.

4 Conclusions

The possibility of two welding processes of connecting the TC4 Ti alloy to SUS 301L stainless steel with Nb sheet as interlayer was studied. The main conclusions are presented below.

The Ti alloy-Nb-SS joint with higher performance was obtained by one-pass welding. The unmelted Nb acted as a diffusion barrier between Ti and Fe avoiding formation of the Ti-Fe intermetallics. The joint comprised a weld zone formed by fusion welding at the Ti alloy-Nb interface, and a reaction layer was formed by eutectic at the Nb-SS interface. No intermetallics except for Ti-Nb solid solution were produced in the weld zone, and columnar grains were observed. Excellent metallurgical bonding was obtained between Ti alloy and Nb interlayer. XRD analysis results confirmed the presence of Fe_7Nb_6 and Fe_2Nb in the reaction layer. In this case, the fracture during tensile test occurred at the reaction layer. The mechanical property of the joint was determined by the reaction layer. The joint fractured at the reaction layer with the maximum tensile strength of 370 MPa and elongation of 1%.

Two-pass welding was applied and two weld zones were produced. The unmelted Nb interlayer acted as a barrier to mix the two base materials during welding. XRD analysis results confirmed the presence of (Ti, Nb) solid solution in WZ_1 and the presence of γ-Fe and Fe_2Nb in WZ_2. However, the creation of two weld zones showed no advantage to improve the mechanical property of the Ti alloy-Nb-SS joint due to formation of γ-Fe and Fe_2Nb intermetallic at the Nb-SS interface. Great hardness difference between them easily led to stress concentration. Poor metallurgical bonding was obtained between the Nb interlayer and stainless steel for two-pass welding. At this point, the tensile strength of joint B was determined by WZ_2 and only 171 MPa and elongation of 0.6% were reached.

References

1. Cherepanov AN, Mali VI, Maliutina IN, Orishich AM, Malikov AG, Drozdov VO (2017) Laser welding of stainless steel to titanium using explosively welded composite inserts. Int J Adv Manuf Technol 90:3037–3043
2. Sun Z, Karppi R (1996) The application of electron beam welding for the joining of dissimilar metals: an overview. J Mater Process Technol 59:257–267
3. Murray JL (1987) Phase diagrams of binary titanium alloys. ASM, International. 99–111
4. Akbari Mousavi SAA, Sartangi PF (2008) Effect of post-weld heat treatment on the interface microstructure of explosively welded titanium-stainless steel composite. Mater Sci Eng A 494:329–336
5. Shuhai C, Mingxin Z, Jihua H (2014) Microstructures and mechanical property of laser butt welding of titanium alloy to stainless steel. Mater Des 53:504–511
6. Kundu S, Chatterjee S (2008) Characterization of diffusion bonded joint between titanium and 304 stainless steel using a Ni interlayer. Mat Charact 59:631–637
7. Kundu S, Chatterjee S (2006) Interfacial microstructure and mechanical properties of diffusion-bonded titanium-stainless steel joints using a nickel interlayer. Mater Sci Eng A 425:107–113
8. Kundu S, Chatterjee S (2010) Evolution of interface microstructure and mechanical properties of titanium/304 stainless steel diffusion bonded joint using Nb interlayer. ISIJ Int 50:1460–1465
9. Lee JG, Hong SJ, Lee MK, Rhee CK (2009) High strength bonding of titanium to stainless steel using an Ag interlayer. J Nucl Mater 395:145–149

10. Wang T, Binggang Z, Jicai F, Qi T (2012) Effect of a copper filler metal on the microstructure and mechanical properties of electron beam welded titanium-stainless steel joint. Mater Charact 73:104–113
11. Ting W, Binggang Z, Guoqing C, Jicai F, Qi T (2010) Electron beam welding of Ti-15-3 titanium alloy to 304 stainless steel with copper interlayer sheet. Trans Nonferrous Met Soc China 20:1829–1834
12. Tomashchuk I, Sallamand P, Belyavina N, Pilloz M (2013) Evolution of microstructures and mechanical properties during dissimilar electron beam welding of titanium alloy to stainless steel via copper interlayer. Mater Sci Eng A 585:114–122
13. Li H, Sun D, Gu X, Dong P, Lv Z (2013) Effects of the thickness of Cu filler metal on the microstructure and properties of laser-welded TiNi alloy and stainless steel joint. Mater Des 50:342–350
14. Yao C, Xu B, Zhang X, Huang J, Fu J, Wu Y (2009) Interface microstructure and mechanical properties of laser welding copper-steel dissimilar joint. Laser Eng Opt 47:807–814
15. Tomashchuk I, Sallamand P, Andrzejewski H, Grevey D (2011) The formation of intermetallics in dissimilar Ti6Al4V/copper/AISI 316L electron beam and Nd:YAG laser joints. Intermetallics 19:1466–1473
16. Yan Z, DaQian S, XiaoYan G, YaJun L (2017) Nd/YAG pulsed laser welding of TC4 titanium alloy to 301L stainless steel via pure copper interlayer. Int J Adv Manuf Technol 90:953–961
17. Yan Z, DaQian S, XiaoYan G, HongMei L (2016) A hybrid joint based on two kinds of bonding mechanisms for titanium alloy and stainless steel by pulsed laser welding. Mater Lett 185:152–155
18. Zongan L, Guanglei W, Guangming X, Lipeng W, Kun Z (2013) Interfacial microstructure and properties of a vacuum hot roll-bonded titanium-stainless steel clad plate with a Nb interlayer. Acta Metall Sin 26:754–760
19. Kundu S, Chatterjee S (2011) Effects of temperature on interface microstructure and strength properties of titanium-Nb stainless steel diffusion bonded joints. Mater Sci Tech-Lond 27:1177–1182
20. Cardarelli F (2008) Materials handbook: a concise desktop reference, second edn. Springer, London
21. Oliveira JP, Panton B, Zeng Z, Andrei CM, Zhou Y, Miranda RM, Braz Fernandes FM (2016) Laser joining of NiTi to Ti6Al4V using a Nb interlayer. Acta Mater 105:9–15
22. Kundu S, Chatterjee S (2010) Interface microstructure and strength properties of diffusion bonded joints of titanium-Al interlayer-18Cr-8Ni stainless steel. Mater Sci Eng A 527:2714–2719
23. Li HM, Sun DQ, Dong P, Wang WQ, Yin SQ (2011) Study on laser welding of dissimilar materials between TiNi shape memory alloy/stainless steel. J Mater Eng Perform 10:47–52
24. Torkamany MJ, Malek Ghainin F, Poursalehi R (2016) An insight to the mechanism of weld penetration in dissimilar pulsed laser welding of niobium and Ti-6Al-4V. Opt Laser Technol 79:100–107
25. Torkamany MJ, Malek Ghaini F, Poursalehi R (2014) Dissimilar pulsed Nd:YAG laser welding of pure niobium to Ti-6Al-4V. Mater Des 53:915–920
26. Pitscheneder W, DebRoy T, Mundra K, Ebner R (1996) Role of sulfur and processing variables on the temporal evolution of weld pool geometry during multikilowatt laser beam welding of steels. Weld J 71–75
27. Zhao X, Kwakernaak C, Pan Y, Richardson IM, Saldi Z, Kenjeres S (2010) The effect of oxygen on transitional Marangoni flow in laser spot welding. Acta Mater 58:6345–6357
28. Dongsheng Z, Jiuchun Y, Yujun L, Zhuoshang J (2014) Interfacial structure and mechanical properties of hot-roll bonded joints between titanium alloy and stainless steel using Nb interlayer. Trans Nonferrous Met Soc China 24:2839–2844
29. Balam SK, Paul A (2010) Interdiffusion study in the Fe-Nb system. Metall Mat Trans A 41:2175–2179